Analysis of the inverse Swift effect using a rate-sensitive polycrystal model

Giessen, Erik van der; Neale, Kenneth W.

Published in:
Computer Methods in Applied Mechanics and Engineering

DOI:
10.1016/0045-7825(93)90050-8

Publication date:
1993

Computer Methods in Applied Mechanics and Engineering 103 (1993) 291–313
North-Holland

CMA 393

Analysis of the inverse Swift effect using a rate-sensitive polycrystal model

Erik van der Giessen
Delft University of Technology, Laboratory for Engineering Mechanics, Delft, The Netherlands

Kenneth W. Neale
Université de Sherbrooke, Faculté des Sciences Appliquées, Sherbrooke, Québec, Canada

Received 13 October 1992
Revised manuscript received 7 December 1992

Complementary to the Swift effect, namely the elongation of specimens during large strain elastic-plastic torsion with free ends, the inverse Swift effect refers to the free twisting of specimens during uniaxial tension after a previous large strain twisting history. In this paper, this intriguing phenomenon in solid cylindrical bars or wires is studied numerically using special purpose finite elements that allow for an accurate and efficient analysis of large strain torsion and simultaneous tension problems. The constitutive model used is a micromechanics polycrystal model based on a large strain crystal plasticity model accounting for rate-sensitive crystallographic slip in face-centered cubic crystals. The description of crystallographic texture development during all stages of the deformation process is inherent in the model. The influence of the material strain-rate sensitivity on the inverse Swift effect is investigated for varying amounts of shear strain imposed during pre-twisting. The simulations are compared with experimental results for copper wires reported in the literature. The marked sensitivity to initial textures as well as a number of constitutive assumptions are discussed in connection with the observed differences between theoretical predictions and experimental observations.

1. Introduction

When a cylindrical bar or tube of a polycrystalline metal is subjected to torsion up to large plastic strains while the ends are left free to displace axially, it exhibits a significant axial lengthening in most cases. This effect was first observed by Swift in 1947 [1]. Recently, it has been shown that crystallographic texture development is the major origin of the Swift effect (see, e.g., [2, 3]). In some cases, shortening occurs or lengthening is followed by shortening during continued twisting; this has been attributed to recrystallization at high homologous temperatures (see, e.g., [4]).

A related phenomenon that has been observed experimentally only very recently, is the so-called inverse Swift effect [5]. Wires of copper were first twisted to large shear strains under free-end conditions. After unloading, these pre-twisted specimens were subjected subsequent-

Correspondence to: Erik van der Giessen, Delft University of Technology, Laboratory for Engineering Mechanics, Postbox 5033, 2600 GA Delft, The Netherlands.

ly to uniaxial tension while they were left free to twist. It was found that at room temperature, such pre-twisted specimens untwisted first, followed by twisting in the same direction as during pre-twisting. It was suggested in [5] that this inverse Swift effect was also mainly due to crystallographic texture; first of all, the texture induced by twisting, and next its further evolution during tension. However, a detailed quantitative analysis of this phenomenon is still lacking.

Both the original and the inverse Swift effect pertain to second-order effects. Any theoretical prediction of such phenomena is well-known to be sensitive to the constitutive modelling employed. Therefore, apart from these effects being particularly intriguing, their investigation is motivated by the fact that they present themselves as sensitive test cases for constitutive models.

In this paper, we report a first numerical study of the inverse Swift effect by means of a polycrystal model that rigorously accounts for the development of crystallographic texture. To be more specific, the model is based on a Taylor model incorporating rate-sensitive crystal plasticity that has been used previously [6] to study fixed-end torsion of solid bars, but extended to include anisotropic elasticity of the crystallites as well as slip system hardening, similar to that of Asaro and Needleman [7].

Twisting of a bar or wire with a solid cross-section involves deformation and stress gradients along the radius of the specimen, while tension of a pre-twisted bar with its inhomogeneous deformation history and internal stresses also causes radial stress gradients. Any quantitative treatment of the problem needs to account for this radial inhomogeneity. Here, the specimen is modelled by means of special purpose, tubular finite elements which extend previously designed elements for large strain torsion only [8]. The Taylor model is implemented locally at each sampling point in the finite element. For each sampling point, the present analyses use an FCC polycrystal with various initial crystallite orientation distributions. In a preliminary study [9], this numerical method has been applied to investigate the standard Swift effect in solid bars as a complement to the homogeneous shearing study in [3].

Due to the rate-sensitive crystallographic slip constitutive equations, the governing equations are highly nonlinear. In order to increase the stable time step size, we use a rate tangent scheme proposed in [10]. Moreover, an adaptive time stepping method is discussed which ensures that increments of several pertinent quantities remain within user-defined bounds.

Standard tensor analysis is used throughout. Tensors and vectors are denoted by boldface letters and $\otimes$ denotes the tensor product. The following operations for arbitrary second-order tensors $\boldsymbol{a}$ and $\boldsymbol{b}$ apply: $\boldsymbol{ab} = a_{ik}b_{kj}\boldsymbol{e}_i \otimes \boldsymbol{e}_j$, $\boldsymbol{a} \cdot \boldsymbol{b} = a_{ij}b_{ij}$, with proper extension to higher-order tensors ($\{\boldsymbol{e}_i\}$ is a Cartesian basis). Latin indices range from 1 to 3, and repeated Latin indices are always summed; Greek indices are not summed. Matrices or component vectors are denoted non-bold. Superscripts t and -1 denote the transverse and inverse of a second-order tensor or matrix, respectively, tr denotes the trace and a superposed dot denotes the material time derivative or rate.

2. Some experimental results

Shrivastava et al. [5] apparently were the first to systematically investigate the inverse Swift effect in solid bars. Their experiments were carried out as follows. Annealed copper wires of 1

to 2 mm in diameter and about 1 m long were first pre-twisted to various amounts of shear and then unloaded, while the wires were left free to elongate or contract axially. Two kinds of pre-twist treatments were carried out: one at room temperature (20 °C) where the shears varied between 5% and 20%, and the other set were performed at 250 and 350 °C, where shears up to 3.0 were possible. The room temperature experiments exhibited the Swift effect, i.e., monotonic elongation with ongoing twist (cf., e.g. [1, 2]). The elevated temperatures correspond to homologous temperatures of 0.39 and 0.46, respectively, and led to shortening of the wire during twisting, indicating the occurrence of dynamic recrystallization (see also [4]). Similar experiments at room temperature on lead wires, corresponding to a homologous temperature of 0.42, also showed shortening. After pre-twisting at the high homologous temperatures, the wires were quenched.

The pre-twisted wires were then subjected to uniaxial tension in a special loading frame that allowed free twisting. Figure 1 shows two typical results of such a test in terms of the shear Γ' at the outer surface of the wire versus the axial strain ε' both measured relative to the unloaded pre-twisted state: one for a wire pre-twisted at room temperature and one for a high temperature pre-twisted wire. In contrast to the monotonic lengthening during twisting, the room temperature wires exhibited negative shearing first, i.e. twisting opposite to that imposed during pre-twisting, followed by positive twisting at larger strains up to failure (at extensions of about 20–30%). The transition from untwisting to twisting appeared to occur once the extension behaviour had become fully plastic, and negative shears of up to -0.1% were observed. By contrast, the wires that were pre-twisted at elevated temperatures exhibited untwisting only.

These observed inverse Swift effects were explained qualitatively in [5] in terms of yield surfaces. The forward twisting behaviour during the moderate strain stages was explained in terms of the texture produced during pre-twisting. The initial untwisting was suggested to

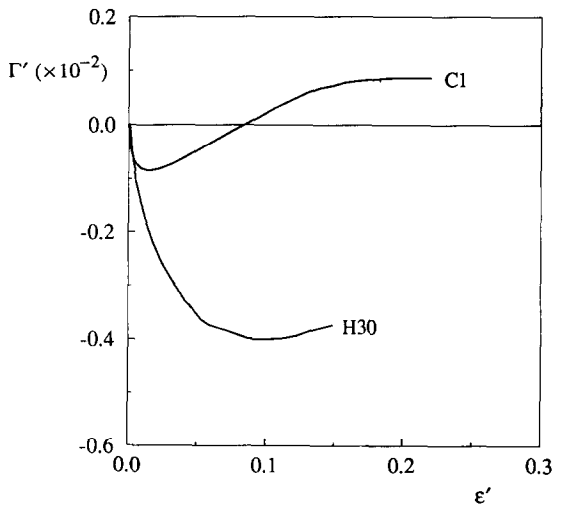

Fig. 1. A few experimental results concerning the inverse Swift effect plotted as the shear strain Γ' at the surface of the wire versus the applied tensile strain ε' (from [5]). 'C1' is a result for a copper wire pre-twisted at 20 °C until $\Gamma_0 = 0.089$ and 'H30' is for a copper wire pre-twisted at 250 °C until $\Gamma_0 = 2.8$. Tension was performed at 20 °C in both cases.

result from micro-Bauschinger effects. The untwisting behaviour in the high temperature pre-twisted specimens was also explained from the induced textures, which are known to be drastically different from the room temperature torsion textures. However, no quantitative attempts were made in [5], nor has that been done elsewhere to the authors' knowledge.

3. The rate-sensitive polycrystal model

In the present work, plastic deformation of a polycrystalline metal is described in terms of a physically motivated crystal plasticity theory where it is implicit that plastic deformation is due solely to crystallographic slip. Various different models of that kind have been proposed in the literature over the years; here, we adopt a rate-sensitive model in a form proposed by Asaro and Needleman [7] and used subsequently in a number of related studies (see, e.g., [3, 6, 9]). We start out by a brief recapitulation of the kinematics and the constitutive equations for a single crystal.

The total deformation of a crystallite is the result of two distinct physical mechanisms: crystallographic slip due to dislocation motion on the active slip systems and elastic lattice distortion. Slip system α of the crystal is defined by the orthonormal pair $(\boldsymbol{s}_\alpha, \boldsymbol{m}_\alpha)$ comprising the unit vector $\boldsymbol{s}_\alpha$ in the slip direction and the unit normal $\boldsymbol{m}_\alpha$ to the slip plane, both measured in the initial configuration. Here we shall focus on cubic materials with a face centered lattice structure; such FCC crystallites possess 12 slip systems of the type $\{1\,1\,1\}\langle 1\,1\,0\rangle$. Plastic deformation of the crystal is envisaged to occur as a set of plastic simple shears along the various slip systems, leaving the lattice and the slip systems' vectors $(\boldsymbol{s}_\alpha, \boldsymbol{m}_\alpha)$ not only essentially undistorted but also unrotated. Next, the material and the lattice deform elastically and rotate rigidly from this plastically deformed state to the actual current configuration. Rice and Asaro [11, 12] formulated this mathematically in terms of the multiplicative decomposition

$$\boldsymbol{F} = \boldsymbol{F}^*\boldsymbol{F}^{\mathrm{p}} \tag{1}$$

of the deformation gradient $\boldsymbol{F}$ into a plastic part $\boldsymbol{F}^{\mathrm{p}}$, due to crystallographic slip, and a part $\boldsymbol{F}^*$ describing the elastic distortion of the lattice. Hence, $\boldsymbol{F}^*$ also includes the rigid rotation of the lattice from its fixed orientation in the plastically deformed configuration to the actual orientation. Straightforward time differentiation of (1) leads to the following decomposition of the velocity gradient:

$$\boldsymbol{L} = \dot{\boldsymbol{F}}\boldsymbol{F}^{-1} = \boldsymbol{L}^* + \boldsymbol{L}^{\mathrm{p}},$$

where

$$\boldsymbol{L}^* = \dot{\boldsymbol{F}}^*\boldsymbol{F}^{*-1}, \quad \boldsymbol{L}^{\mathrm{p}} = \boldsymbol{F}^*\boldsymbol{\Lambda}^{\mathrm{p}}\boldsymbol{F}^{*-1}, \quad \boldsymbol{\Lambda}^{\mathrm{p}} = \dot{\boldsymbol{F}}^{\mathrm{p}}\boldsymbol{F}^{\mathrm{p}-1}. \tag{2}$$

Taking symmetric and skewsymmetric parts, this leads to the elastic strain-rate $\boldsymbol{D}^*$, the plastic strain-rate $\boldsymbol{D}^{\mathrm{p}}$, the plastic spin $\boldsymbol{W}^{\mathrm{p}}$ and the spin $\boldsymbol{W}^*$ associated with the rigid lattice rotation (and with lattice elasticity, though this usually is a much smaller contribution):

$$\boldsymbol{D} = \boldsymbol{D}^* + \boldsymbol{D}^{\mathrm{p}}, \qquad \boldsymbol{W} = \boldsymbol{W}^* + \boldsymbol{W}^{\mathrm{p}}. \tag{3}$$

Taking the slip direction to be convected with the lattice, so that in the current state $\boldsymbol{s}_\alpha^* = \boldsymbol{F}^* \boldsymbol{s}_\alpha$ while $\boldsymbol{m}_\alpha^* = \boldsymbol{m}_\alpha \boldsymbol{F}^{*-1}$ remains orthogonal to $\boldsymbol{s}_\alpha^*$, their evolution is given by

$$\dot{\boldsymbol{s}}_\alpha^* = \boldsymbol{L}^* \boldsymbol{s}_\alpha^*, \qquad \dot{\boldsymbol{m}}_\alpha^* = -\boldsymbol{L}^{*\mathrm{t}} \boldsymbol{m}_\alpha^*. \tag{4}$$

It is of interest to notice here that while the developments of crystal plasticity theories on the one hand and frameworks of large strain phenomenological plasticity on the other have taken place largely independently, the kinematic framework summarized above is completely similar to one in phenomenological plasticity that was proposed originally by Besseling in 1968 [13] and by Mandel in 1971 [14]. The particular feature that these kinematic frameworks have in common is the concept of what Besseling called a 'geometrical natural reference configuration' or what has become better known as Mandel's term 'isoclinic intermediate reference configuration'. Although the precise interpretations may differ, such a configuration is one whose orientation remains the same throughout the deformation process. To monitor the orientation of a local configuration of a material point in a general continuum mechanics setting, Besseling and Mandel attributed to it a local triad of directors, which in the isoclinic configuration then retained fixed directions in space. In crystal plasticity, these directors and the isoclinic configuration gain a clear physical interpretation: as put forward already by Mandel [14], these directors can be identified in the case of a single slip system with the slip direction $\boldsymbol{s}$, slip plane normal $\boldsymbol{m}$ and $\boldsymbol{s} \times \boldsymbol{m}$, while in the case of a single cubic crystal with multiple slip systems, they can be identified simply with the lattice directions. Also in crystal plasticity, the much debated concept of plastic spin gets a clear physical interpretation through the relations (2)–(4) and is constitutively described by the physical process of slip as will be established later, whereas Besseling [13] had to put the plastic spin equal to zero because of lack of a sufficient internal variable structure. More details concerning a possible reconciliation of these aspects may be found in [15].

In the formulation of the constitutive description, we introduce, as in [3, 7, 10], the following symmetric and antisymmetric tensors for each slip system:

$$\boldsymbol{P}_\alpha = \tfrac{1}{2}[\boldsymbol{s}_\alpha^* \otimes \boldsymbol{m}_\alpha^* + \boldsymbol{m}_\alpha^* \otimes \boldsymbol{s}_\alpha^*], \qquad \boldsymbol{W}_\alpha = \tfrac{1}{2}[\boldsymbol{s}_\alpha^* \otimes \boldsymbol{m}_\alpha^* - \boldsymbol{m}_\alpha^* \otimes \boldsymbol{s}_\alpha^*]. \tag{5}$$

For a given crystal the plastic strain-rate and spin are then, respectively, given by

$$\boldsymbol{D}^{\mathrm{p}} = \sum_\alpha \boldsymbol{P}_\alpha \dot{\gamma}_\alpha, \qquad \boldsymbol{W}^{\mathrm{p}} = \sum_\alpha \boldsymbol{W}_\alpha \dot{\gamma}_\alpha, \tag{6}$$

where $\dot{\gamma}_\alpha$ is the shear rate on slip system α.

The elastic constitutive equation for a crystal is specified by

$$\overset{\nabla}{\boldsymbol{\tau}}{}^* = \dot{\boldsymbol{\tau}} - \boldsymbol{W}^* \boldsymbol{\tau} + \boldsymbol{\tau} \boldsymbol{W}^* = \mathscr{L}^0 \boldsymbol{D}^*, \tag{7}$$

where $\mathscr{L}^0$ is the tensor of elastic moduli and $\overset{\nabla}{\boldsymbol{\tau}}{}^*$ is the Jaumann rate of Kirchhoff stress based on the lattice rotations. Here, the tensor $\mathscr{L}^0$ is based on the anisotropic elastic constants for an FCC crystal and thus exhibits the appropriate cubic symmetry. Combining (7) with (3) to (6),

the constitutive equation for the crystal in terms of the Jaumann rate based on the continuum spin $\boldsymbol{W}$ is found in the form [3, 7, 10]

$$\overset{\nabla}{\boldsymbol{\sigma}} = \mathscr{L}^0 \boldsymbol{D} - \dot{\boldsymbol{\sigma}}^0 - \boldsymbol{\sigma}\,\mathrm{tr}\,\boldsymbol{D}\,, \tag{8}$$

where $\dot{\boldsymbol{\sigma}}^0$ is a visco-plastic type stress rate defined by

$$\dot{\boldsymbol{\sigma}}^0 = \sum_\alpha \boldsymbol{R}_\alpha \dot{\gamma}_\alpha\,, \qquad \text{with } \boldsymbol{R}_\alpha = \mathscr{L}^0 \boldsymbol{P}_\alpha + \boldsymbol{W}_\alpha \boldsymbol{\sigma} - \boldsymbol{\sigma} \boldsymbol{W}_\alpha\,. \tag{9}$$

Here we have immediately expressed the relationship in terms of the Cauchy stress rather than the Kirchhoff stress $\boldsymbol{\tau} = (\det \boldsymbol{F})\boldsymbol{\sigma}$, using the fact that the relative volume change $\det \boldsymbol{F} - 1$ is entirely due to elastic strains, which remain small.

With the rate-sensitive crystal plasticity model employed, the slip rates are governed by the power-law expression

$$\dot{\gamma}_\alpha = \dot{\gamma}_0\,\mathrm{sgn}(\tau_\alpha)\left|\frac{\tau_\alpha}{g_\alpha}\right|^{1/m}. \tag{10}$$

In this relation, τ_α is the resolved shear stress on slip system α and g_α is its hardness. The resolved shear stress is related to the Cauchy stress $\boldsymbol{\sigma}$ through

$$\tau_\alpha = \boldsymbol{P}_\alpha \cdot \boldsymbol{\sigma}\,.$$

In the present analysis, isotropic slip system hardening will be assumed, although it is a straightforward matter to include other models which account for latent hardening. Accordingly, g_α is taken to be identical for each system. The following form is adopted [3]:

$$g_\alpha = \tau_0 + h_s \gamma + (\tau_s - \tau_0)\tanh\left[\frac{h_0 - h_s}{\tau_s - \tau_0}\,\gamma\right], \quad \text{where } \gamma = \sum_\alpha |\gamma_\alpha| \tag{11}$$

represents the accumulated sum of slips on all slip systems. In (11), τ_0 is an initial critical shear stress, and h_0 and h_s are material constants representing the initial and asymptotic hardening rates, respectively. If $h_s = 0$, τ_s represents the saturation value of the shear stress.

The polycrystal response is obtained by invoking the Taylor assumption. Thus, the deformation in each grain comprising the polycrystal is taken to be identical to that imposed macroscopically on the polycrystal. The macroscopic values of all quantities such as stresses $\boldsymbol{\sigma}$, stress rates $\dot{\boldsymbol{\sigma}}$, $\dot{\boldsymbol{\sigma}}^0$ and elastic moduli $\mathscr{L}^0$ are obtained by averaging the particular values $\boldsymbol{\sigma}^{(k)}$, $\dot{\boldsymbol{\sigma}}^{(k)}$, $\dot{\boldsymbol{\sigma}}^{0(k)}$, $\mathscr{L}^{0(k)}$ for each crystal k over the total number of grains, N, in the polycrystal.

4. Method of analysis

4.1. Formulation of the problem

We consider a solid, circular cylindrical bar (or wire) with an initial radius R_0 and initial length L_0 subject to, in general, a combination of twisting and axial extension. The kinematics

involved, subject to rather mild assumptions to be discussed later, can be summarized as follows (see, e.g., [6, 16]). If the initial cylindrical coordinates of a material point are $X^i = (r_0, \theta_0, z_0)$, its coordinates in a deformed configuration $x^i = (r, \theta, z)$ at time t are given by

$$r = r(r_0; t)\,, \quad \theta = \theta_0 + \omega(t) z_0\,, \quad z = e(t) z_0\,,$$

with $\omega = \varphi / L_0$ the angle of twist per unit initial length L_0 over which all points in a cross-section are rotated, and with e the extensional stretch in the axial direction z. Adopting a spatially fixed orthonormal basis $\{\boldsymbol{e}_i\}$ associated with x^i, so that tensor components with respect to this basis represent physical components, the components of the strain-rate tensor $\boldsymbol{D} = D_{ij} \boldsymbol{e}_i \otimes \boldsymbol{e}_j$ and the spin tensor $\boldsymbol{W} = W_{ij} \boldsymbol{e}_i \otimes \boldsymbol{e}_j$ read

$$D_{11} = \frac{\partial \dot{r}}{\partial r}\,, \quad D_{22} = \frac{\dot{r}}{r}\,, \quad D_{33} = \frac{\dot{e}}{e}\,, \quad D_{23} = \frac{1}{2}\,\frac{r\dot{\omega}}{e}\,, \quad D_{12} = D_{13} \equiv 0\,;$$

$$W_{12} = -\,\frac{z\dot{\omega}}{e}\,, \quad W_{13} = 0\,, \quad W_{23} = \frac{1}{2}\,\frac{r\dot{\omega}}{e}\,.$$

Accordingly, plane cross-sections of the bar remain plane throughout the deformation and the state of deformation is homogeneous in the axial direction. Hence, the instantaneous geometry is completely specified by the current radius R and length L. It should be realized that this simple state of deformation tacitly assumes that the behaviour of the bar remains axisymmetric; that is, even though texture development will take place with the constitutive model discussed previously, all properties can depend only on the radial direction. This state of deformation will be distorted somewhat in the neighbourhood of the unavoidable grips of the specimen, but when the strains and twist are measured over a purely prismatic part located sufficiently far away from the ends, as in [17], or when their influence can be regarded to be negligible when using wires, as in [5], this is expected to be sufficiently accurate for present purposes.

The problem is governed by the components of the Cauchy stress tensor $\boldsymbol{\sigma} = \sigma_{ij} \boldsymbol{e}_i \otimes \boldsymbol{e}_j$ that are dual to the nonzero components of $\boldsymbol{D}$, that is, σ_{11}, σ_{22}, σ_{23}, σ_{33}. Due to axisymmetry and axial homogeneity, these components depend only on the radial coordinate, $\sigma_{ij} = \sigma_{ij}(r)$, while $\sigma_{13} = 0$. For isotropic materials and for orthotropic materials with their principal axes along the x^i, one also has $\sigma_{12} = 0$; with the constitutive model discussed in the foregoing this cannot be guaranteed, but the actual value of σ_{12} is of no concern for the solution of the problem at hand. The lateral surface of the bar will remain stress free, $\sigma_{11}(R) \equiv 0$, while the tractions on the ends of the cylindrical bar will be represented by the axial force F and the torque T defined by

$$F = 2\pi \int_0^R r\sigma_{33}\, \mathrm{d}r\,, \qquad T = 2\pi \int_0^R r^2 \sigma_{23}\, \mathrm{d}r\,.$$

In determining for this problem the contribution from the Jaumann convective terms in the rate constitutive equations (8), it is crucial – yet easily overlooked – to account for the fact that since the $x^i = (r, \theta, z)$ are curvilinear coordinates, the material time derivative of the base vectors $\boldsymbol{e}_i$ does not vanish. As a consequence, the components of the Jaumann stress rate

$\overset{\nabla}{\boldsymbol{\sigma}} = \dot{\boldsymbol{\sigma}} - \boldsymbol{W}\boldsymbol{\sigma} + \boldsymbol{\sigma}\boldsymbol{W}$ are given by (see [18])

$$\overset{\nabla}{\sigma}_{ij} = \dot{\sigma}_{ij} + (H_{ik} - W_{ik})\sigma_{kj} + \sigma_{ik}(H_{jk} - W_{jk}) , \tag{12}$$

where the H_{ij} are the so-called shift rates which, for the kinematics discussed above, yield

$$H_{23} - W_{23} = -(H_{32} - W_{32}) = -\frac{1}{2}\frac{r\dot{\omega}}{e} , \qquad H_{ij} - W_{ij} = 0 \text{ otherwise.}$$

With a view on simulating the experiments of Shrivastava et al. [5], the present computations involve three stages: first, twisting under conditions of free axial extension up to a certain amount of twist, followed by a stage of unloading, and finally, a stage of uniaxial extension with the possibility of free twists. Thus, the following groups of boundary conditions are considered:

$$\begin{aligned} &\text{Stage I: Free-end twisting until } \varphi = \varphi_0\text{:} \quad F = 0 , \quad \dot{\varphi} = \dot{\Phi} ; \\ &\text{Stage II: Untwisting until } T = 0\text{:} \quad F = 0 , \quad \dot{\varphi} = \dot{\Phi} ; \\ &\text{Stage III: Free-twisting extension:} \quad T = 0 , \quad \dot{e}/e = \dot{\varepsilon} ; \end{aligned} \tag{13}$$

where $\dot{\Phi}$ is the prescribed twist rate during twisting (and taken to be equal to the twist-rate during untwisting) and $\dot{\varepsilon}$ is the axial strain-rate during subsequent tension.

4.2. *The finite torsion element*

The problem described above is basically a one-dimensional problem along the r-axis. This can be efficiently handled by means of a slightly extended version of the special purpose finite torsion elements designed by Wu and Van der Giessen [8]. As illustrated in Fig. 2, each element is actually a circular cylindrical tube, but computationally it is considered to be one-dimensional along the r-axis, with two nodes at $r = r_1$ and $r = r_2$, respectively (see Fig. 2(b)). Within each element the radial velocity $v_1 = \dot{r}$ is interpolated through a linear

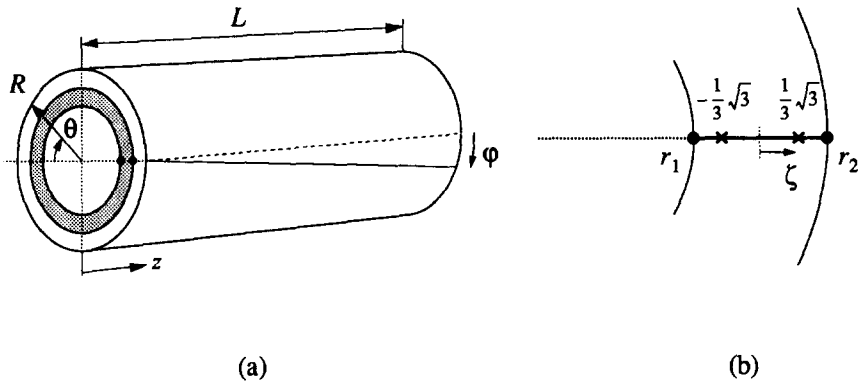

(a) (b)

Fig. 2. (a) The special purpose finite element used for the analysis; (b) shows the nodal points (•) and the material sampling points (×) for each element.

interpolation of the circumferential strain-rate $D_{22} = \dot{r}/r$ between the nodal values $\dot{r}_1/r_1$ and $\dot{r}_2/r_2$. Within each element two material sampling points or integration points are adopted. For more details concerning the precise formulation of the finite element equations, we refer to [8]; suffice it to reiterate here the strain-rate expressions and the instantaneous discrete equilibrium conditions obtained from the principle of virtual work, respectively:

$$\dot{E} = BV\,, \qquad B^{t}\Sigma = F\,.$$

Here, V is the vector of degrees of freedom of the bar (consisting of, say, n elements) and comprises the $n+1$ radial nodal velocities in terms of $\dot{r}_i/r_i$ along with the axial strain-rate $\dot{\varepsilon}$ and the twist rate $\dot{\varphi}$; F is the dual vector containing the nodal radial forces along with the axial force and the torque; $\dot{E}$ is the vector containing the non-zero strain-rate components $\{D_{11}, D_{22}, 2D_{23}, D_{33}\}$ at all sampling points and Σ is the vector of weighted dual stress components $\{\sigma_{11}, \sigma_{22}, \sigma_{23}, \sigma_{33}\}$ at each sampling point. The rate equilibrium equations are obtained by straightforward differentiation,

$$B^{t}\dot{\Sigma} + GV = \dot{F}\,, \tag{14}$$

where the matrix G accounts for the geometrically nonlinear effects contained in B.

4.3. *Implementation of rate-sensitive polycrystal model*

The polycrystal model discussed in Section 3 is implemented in these special elements in the following manner. At each of the two sampling points within each element, the polycrystal model is applied locally. That is, a polycrystalline aggregate of N grains is attributed to each sampling point, and the local sampling point response is taken to be that of the polycrystal in the sense of the Taylor assumption. The $2n$ polycrystals at the sampling points are initialized to have the same random grain orientation distribution in the undeformed state. Note that this procedure is similar to that used in e.g. [19] for more familiar plane strain continuum elements. With each crystal's constitutive equation in the form (8), the constitutive equations for the entire finite element model are of the form

$$\dot{\Sigma} = S^{0}\dot{E} - \dot{\Sigma}^{0} - CV\,, \tag{15}$$

where S^0 is the symmetric constitutive matrix built up from the elastic moduli $\mathscr{L}^0$ of each grain, $\dot{\Sigma}^0$ is the vector composed of the average viscoplastic stress components $\{\dot{\sigma}^0_{11}, \dot{\sigma}^0_{22}, \dot{\sigma}^0_{23}, \dot{\sigma}^0_{33}\}$ according to (9) for each sampling point, and C is a nonsymmetric convective contribution originating from the Jaumann convective terms in (12) and from the dilatational term in (8).

Because of the strong nonlinearity of the plastic shear flow law (10), the integration of the constitutive equations for each crystallite requires special attention in order to ensure numerical stability. The procedure followed here to implement the rate-sensitive crystal plasticity constitutive equations into the finite element equations uses the one-step, explicit rate tangent method described by Pierce et al. [10]. This method falls within the category of forward gradient methods for the integration of nonlinear constitutive rate equations, as

discussed nowadays in text books like [20]. The particular crystal plasticity formulation implies that all quantities be integrated using the Euler forward scheme based on the corresponding rates at time t, except for the slip γ_α on each slip system. Instead, the slip increment $\Delta\gamma_\alpha = \gamma_\alpha^{t+\Delta t} - \gamma_\alpha^t$ on slip system α for the time increment Δt is specified through the linear interpolation

$$\Delta\gamma_\alpha = [(1-\theta)\dot{\gamma}_\alpha^t + \theta\dot{\gamma}_\alpha^{t+\Delta t}]\Delta t\,, \tag{16}$$

so that it accounts for the change in shear rate $\dot{\gamma}_\alpha$ during the time increment. The parameter θ ranges from 0 to 1; $\theta = 0$ corresponds to the Euler forward scheme. The slip rate at time $t + \Delta t$ is estimated using a so-called forward gradient approach based on a Taylor expansion of (10):

$$\dot{\gamma}_\alpha^{t+\Delta t} = \dot{\gamma}_\alpha^t + \left(\frac{\partial\dot{\gamma}_\alpha}{\partial\tau_\alpha}\,\dot{\tau}_\alpha + \frac{\partial\dot{\gamma}_\alpha}{\partial g_\alpha}\,\dot{g}_\alpha \right)\Big|_t \Delta t\,.$$

Ultimately, the slip increment according to (16) can be expressed in terms of quantities at time t as

$$\Delta\gamma_\alpha = (\dot{f}_\alpha + \boldsymbol{F}_\alpha \cdot \boldsymbol{D})\Delta t\,, \tag{17}$$

where

$$\dot{f}_\alpha = \sum_\beta M_{\alpha\beta}\dot{\gamma}_\beta^t\,, \qquad \boldsymbol{F}_\alpha = \sum_\beta M_{\alpha\beta}\boldsymbol{Q}_\beta\,, \qquad \boldsymbol{Q}_\alpha = \left(\frac{\theta\dot{\gamma}_\alpha^t \Delta t}{m\tau_\alpha} \right)\boldsymbol{R}_\alpha\,,$$

and where $M_{\alpha\beta}$ is the inverse of the matrix $N_{\alpha\beta}$ defined by

$$N_{\alpha\beta} = \delta_{\alpha\beta} + \left(\frac{\theta\dot{\gamma}_\alpha^t \Delta t}{m\tau_\alpha} \right)\left[\boldsymbol{R}_\alpha \cdot \boldsymbol{P}_\beta + \mathrm{sgn}(\tau_\beta) h_{\alpha\beta} \frac{\tau_\alpha}{g_\alpha} \right]. \tag{18}$$

With the slip increment according to (17), the Euler forward incremental form of the crystal constitutive equations (8) becomes [10]

$$\overset{\nabla}{\boldsymbol{\sigma}}\Delta t = \mathscr{L}(\boldsymbol{D}\Delta t) - \Delta\boldsymbol{\sigma}_0 - \boldsymbol{\sigma}(\mathrm{tr}\,\boldsymbol{D}\,\Delta t)\,, \tag{19}$$

with

$$\mathscr{L} = \mathscr{L}^0 - \sum_\alpha \boldsymbol{R}_\alpha \otimes \boldsymbol{F}_\alpha\,, \qquad \Delta\boldsymbol{\sigma}_0 = \sum_\alpha \boldsymbol{R}_\alpha \dot{f}_\alpha \Delta t\,, \tag{20}$$

and from the associated average constitutive relations for the polycrystal, one then obtains the finite element incremental constitutive relations replacing (15). Substitution into the incremental form of the rate equilibrium equations (14) finally leads to the finite element equations of the form

$$[B^t S B + G - B^t C]V\Delta t = \dot{F}\Delta t + B^t\Delta\Sigma_0 - [B^t\Sigma - F]\,. \tag{21}$$

The matrix S is the nonsymmetric constitutive matrix determined by the moduli $\mathscr{L}$ in (20) and $\Delta\Sigma_0$ comprises contributions from the tensor $\Delta\boldsymbol{\sigma}_0$. The equilibrium conditions in the right-

hand side are included in order to prevent drifting of the solution away from the true equilibrium path. The system's stiffness matrix in the left-hand side is nonsymmetric, but this poses no difficulties for the present elements which with their minimal bandwidth allow for a simple efficient solution procedure.

The rate tangent formulation of the crystal constitutive equations in the form (19), (20) has been successfully used in a number of numerical studies of the plastic deformation of crystals or polycrystals, such as [3, 7]. A fully implicit integration scheme, which requires a more elaborate analysis, is discussed in [28].

Once the incremental changes of the degrees of freedom, including the axial strain increment $\Delta\varepsilon$ and twist increment $\Delta\varphi$, are solved from (21), the slip increments are obtained from (17), and all other constitutive quantities can be updated in a straightforward manner. The stresses in each crystallite are updated from (19) and after that the new lattice geometry is found from (4) (see [10]). Finally, the specimen's geometry is updated and the global torque and axial force are computed from the crystallite stresses.

The time step size Δt to be used for each increment is determined adaptively through an automatic procedure consisting of three key parts.

Part 1. The first two steps of each new loading sequence are performed with very small time steps such that any plastic deformation is excluded, and the 'elastic' stress state is obtained for the present loading conditions. For the present computations this procedure is applied at the beginning of each of the three stages in (13). In the case of stages II or III, residual stresses will be present in the crystallites ($\boldsymbol{\sigma}^{(k)} \neq \mathbf{0}$), and they will of course be part of this stress state. The size of the time step is defined as a small fraction of a reference time scale t_R,

$$\Delta t = 10^{-8} t_R\,, \quad t_R = \frac{1}{C_{44}} \frac{\tau_0}{\dot{\Gamma}} \left(\frac{\dot{\Gamma}}{\dot{\gamma}_0} \right)^m\,,$$

which, in a loose sense, relates the viscoplastic shear rate $\dot{\Gamma} = \sqrt{2\mathrm{tr}\,\boldsymbol{D}^2}$ according to a power-law of the type (10) with the elastic shear under the same stress.

Part 2. At the beginning of the third time step, the time increment is determined on the basis of a prescribed work rate per unit volume, $W = (\dot{F}^t V \Delta t)/(\pi R_0^2 L_0)$, during that step. The applied work rate is estimated on the basis of the 'elastic' stress state determined as discussed above, and W is scaled with the elastic shear modulus C_{44}, i.e. $W \equiv \varepsilon_W C_{44}$. Thus, the time increment is obtained from

$$\Delta t = \varepsilon_W \pi R_0^2 L_0 \frac{C_{44}}{\dot{F}^t V}\,,$$

and its size is controlled by the parameter ε_W.

Part 3. During all subsequent increments, a maximum allowable time step Δt_m is determined at various stages during the numerical procedure as the maximum value of $\Delta t'$ computed from each of the following criteria:

$$\Delta t' \leqslant \frac{\Delta\gamma_{\max}}{\dot{\gamma}_\alpha} ;$$

$$\Delta t' \leqslant \varepsilon_g \frac{g_\alpha}{\dot{g}_\alpha} ; \tag{22}$$

$$\Delta t' \leqslant \varepsilon_t t_D , \quad t_D = \frac{m}{\theta \dot{\gamma}_\alpha^t} .$$

The first two criteria ensure that the slip increment and the hardness increment during a time increment $\Delta t'$ do not exceed a maximum slip increment $\Delta\gamma_{\max}$ and a fraction ε_g of the current hardness, respectively. The last criterion ensures that with a sufficiently small value of ε_t, the matrix $N_{\alpha\beta}$ in (18) is invertible (see [10]). If at the end of the increment, $\Delta t'$ is smaller than the current time step Δt, the time step of the next increment is taken equal to $\Delta t'$; if $\Delta t'$ exceeds Δt for a number of consecutive increments (say, five), Δt is increased by a factor 1.5.

Clearly, the procedure is rather heuristic, but is extremely simple to implement in an incremental code. Altogether, this adaptive time step selection procedure involves five parameters, the values of which have to be determined empirically. The results to be presented in the next section have all been obtained with the following values: $\varepsilon_W = 10^{-4}$, $\Delta\gamma_{\max} = 0.0025$, $\varepsilon_g = 0.01$, $\varepsilon_t = 0.05$. These values have been found to ensure numerical stability in all cases to be presented. Several cases have been repeated with half of the above values, and in each case the differences in the global response quantities remained smaller than 0.5%.

5. Results

The problem described in Section 4.1 involves a number of dimensionless groups, and therefore we introduce the following nondimensional quantities:

$$\Gamma = \frac{R_0}{L_0}\varphi , \qquad \bar{\tau} = \frac{3T}{2\pi R_0^3 \tau_0} , \qquad \bar{\sigma} = \frac{F}{\pi R_0^2 \tau_0} ,$$

thus allowing the results to be presented independent of the actual geometry. Here, Γ represents the shear strain at the outer radius of the specimen, provided that geometrical changes remain small, and $\bar{\tau}$ and $\bar{\sigma}$ are the normalized torque and axial force, respectively.

The computations have been carried out by taking a uniform mesh comprising $n = 5$ elements. Previous investigations of solid bar torsion using macroscopic phenomenological constitutive models have shown, by comparison with semi-analytical solutions, that this gives a sufficiently accurate representation of the stress and strain states within the bar [8, 21].

The results to be presented have been obtained by assuming the values $C_{11} = 842\tau_0$, $C_{12} = 607\tau_0$ and $C_{44} = 377\tau_0$ for the cubic elastic constants, representing typical values for copper. Furthermore, we have taken the following material constants: $\tau_s = 1.8\tau_0$, $h_0 = 8.9\tau_0$ and $q = 1.0$, the latter corresponding to isotropic hardening. Most analyses have used $h_s = 0$, but the effect of a small asymptotic hardening rate is also briefly considered. Finally, a range

of values of the rate sensitivity parameter m from $m = 0.005$ to $m = 0.2$ has been employed. Note that all these material parameters correspond to those used in the large strain shear studies in [3] and also in the previous preliminary study of the Swift effect [9]. The reference strain-rate $\dot{\gamma}_0$ in (10) is specified through the time constant $\tau_0/(C_{44}\dot{\gamma}_0) = 2.65$, and the applied strain-rates are specified relative to that value as follows. During the pre-twisting stages I/II in (13), the twist-rate $\dot{\Phi}$ is specified through $\dot{\Gamma} = (R_0/L_0)\dot{\Phi} = 0.75\dot{\gamma}_0$, while during the subsequent tension stage III the strain-rate $\dot{\varepsilon}$ is taken according to $\dot{\varepsilon} = 5\dot{\gamma}_0$. It is difficult to relate these values to the experiments in [5], but it is expected that the results to be reported are not affected much by strain-rates that differ within one or two orders of magnitude.

In this study, we will employ three different polycrystalline aggregates to be attributed to each sampling point in the finite element model of the bar. Each of the aggregates is designed to represent an initially isotropic material; but with the limited number of grains assumed in each aggregate this can only be established approximately. As we will demonstrate later on, the inverse Swift effect appears to be very sensitive to initial anisotropy before the pre-twisting stage, and therefore we will explore this in some detail by considering different polycrystalline aggregates. In accordance with most literature on shear or torsion of FCC polycrystals, the orientation distribution of the grains in the polycrystalline aggregate is conveniently characterized by the stereographic projections of the $\langle 1\,1\,1\rangle$ crystallographic directions on the radial direction $\boldsymbol{e}_1$. The pole figures of the three aggregates studied here are shown in Fig. 3. The distributions with 300 and 500 grains in a polycrystalline aggregate are random, and are observed to lead to a fairly uniform coverage of orientations. The distribution with 400 grains is constructed from a random distribution consisting of 100 grains, which is then symmetrized with respect to each of the coordinate planes. To appreciate the initial degree of isotropy obtained with these distributions, we follow [3] and present in Table 1 the components $\bar{\mathscr{L}}^0_{ijkl}$ of the average elasticity tensor $\bar{\mathscr{L}}^0$ for the aggregate on the basis $\{\boldsymbol{e}_i\}$. The components are

Table 1
Components of the aggregate's average elastic moduli defined in (23)

	400 grains		
1031.1	509.27	0.00	515.65
	1031.2	0.00	515.52
		285.52	0.00
			1024.83
	300 grains		
1036.6	507.58	−1.33	511.84
	1033.0	−0.02	515.46
		285.46	1.35
			1028.7
	500 grains		
1036.0	504.85	−1.86	515.13
	1033.2	0.59	517.96
		287.96	1.26
			1022.9

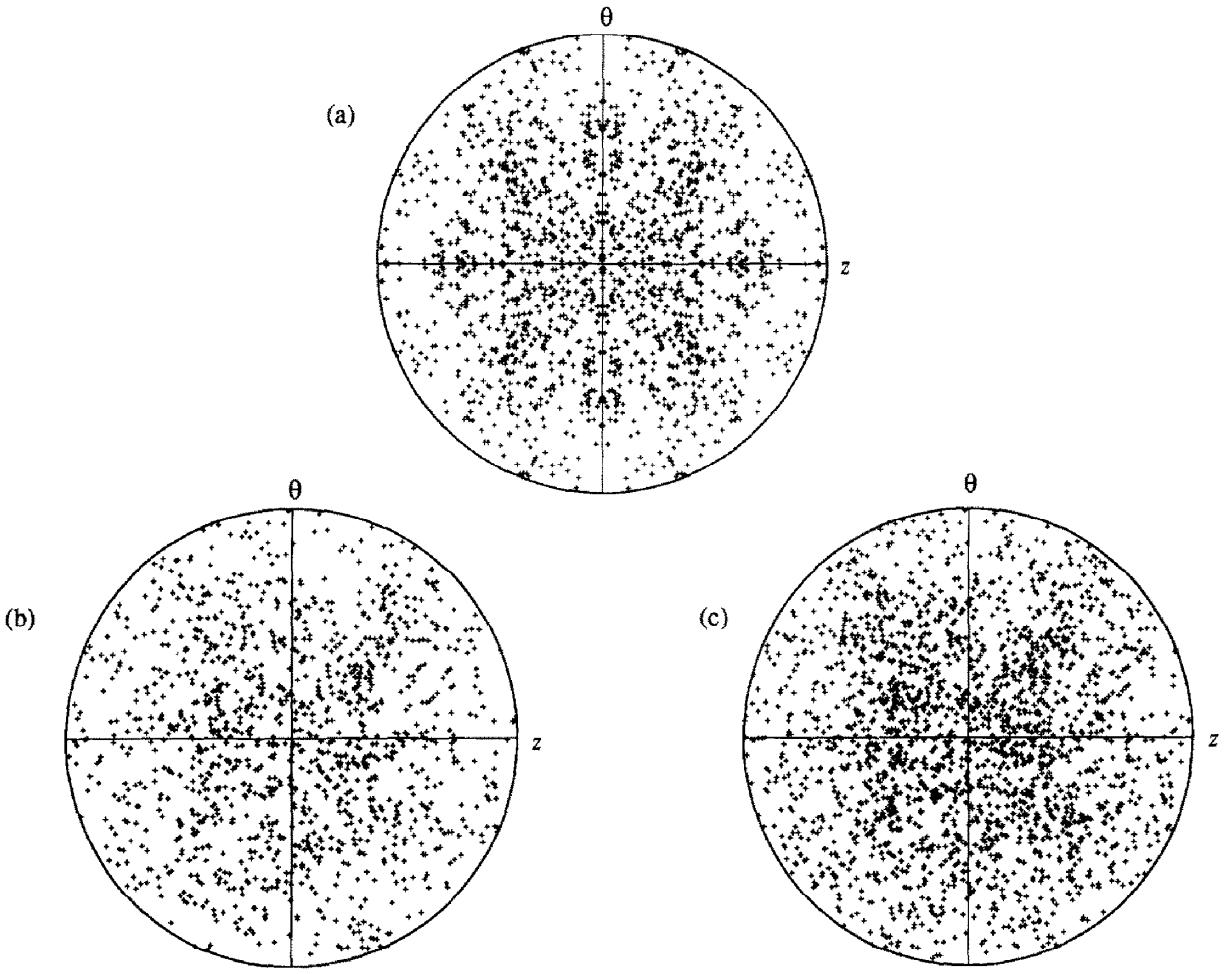

Fig. 3. Initial grain orientation distributions represented by {1 1 1} stereographic pole figures for (a) 400 grains, (b) 300 grains and (c) 500 grains. The θ and z axes correspond to the coordinate system shown in Fig. 2.

presented in the following matrix form:

$$\left[\bar{\mathscr{L}}^0_{ijkl}\right] = \begin{bmatrix} \bar{\mathscr{L}}^0_{1111} & \bar{\mathscr{L}}^0_{1122} & \bar{\mathscr{L}}^0_{1123} & \bar{\mathscr{L}}^0_{1133} \\ & \bar{\mathscr{L}}^0_{2222} & \bar{\mathscr{L}}^0_{2223} & \bar{\mathscr{L}}^0_{2233} \\ & & \bar{\mathscr{L}}^0_{2323} & \bar{\mathscr{L}}^0_{2333} \\ \text{sym} & & & \bar{\mathscr{L}}^0_{3333} \end{bmatrix}, \tag{23}$$

thus containing only those components that are pertinent to the present problem. It is seen that neither one of the distributions produces an isotropic material for which

$$\bar{\mathscr{L}}^0_{1122} = \bar{\mathscr{L}}^0_{1133} = \bar{\mathscr{L}}^0_{2233} = \lambda\,, \quad \bar{\mathscr{L}}^0_{2323} = \mu\,, \quad \bar{\mathscr{L}}^0_{1111} = \bar{\mathscr{L}}^0_{2222} = \bar{\mathscr{L}}^0_{3333} = \lambda + 2\mu\,, \tag{24}$$

with all other components in (23) vanishing, and where λ and μ are the usual isotropic elastic constants. In particular, the '300' and '500' grain distributions involve a certain amount of non-orthotropic response reflected in the coupling between normal and shear components, e.g. $\bar{\mathscr{L}}^0_{2333} = 0.005\bar{\mathscr{L}}^0_{2323}$. This will turn out later to affect our predictions rather strongly. The '400' grain distribution does not involve this coupling, but still does not satisfy the isotropy relations (24).

Figures 4 and 5 show the results of a simulation of the stages I/II and III, respectively,

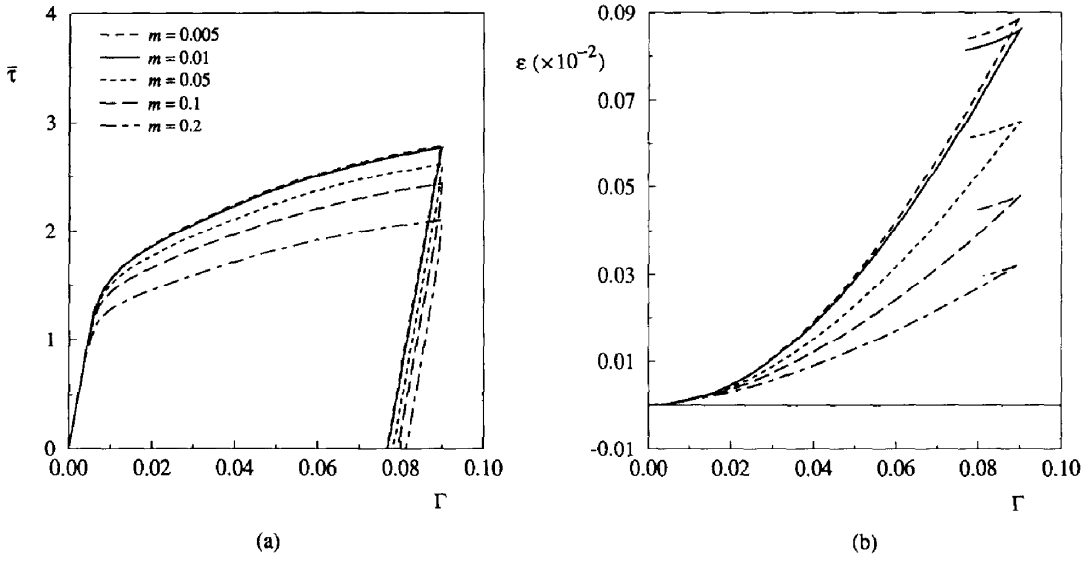

Fig. 4. Torque response (a) and axial strain development (b) during pre-twisting until $\Gamma_0 = 0.09$ for various values of m using the '400' grain distribution.

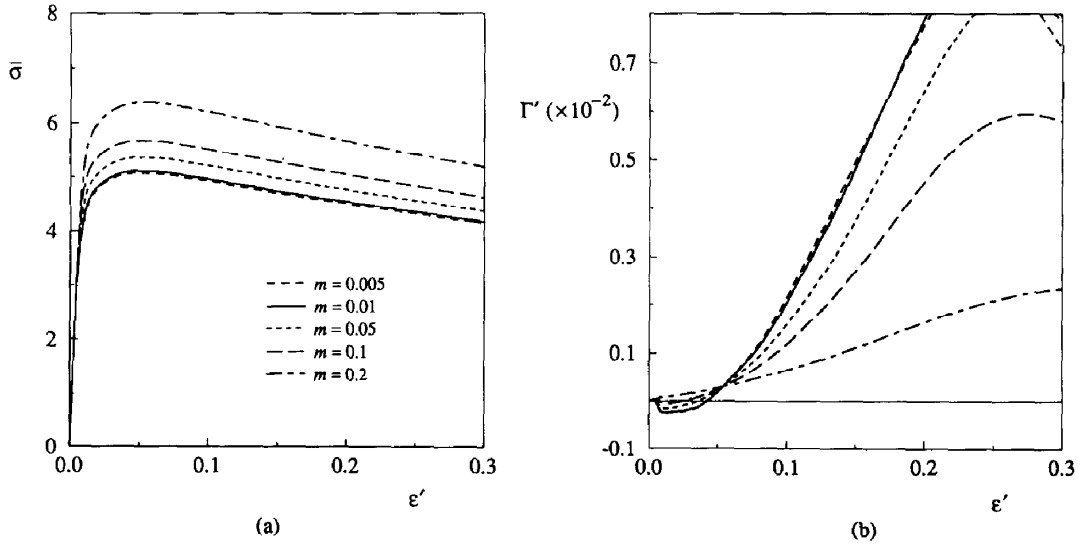

Fig. 5. Axial force response (a) and twist (b) during uniaxial tension from the corresponding pre-twisted states ($\Gamma_0 = 0.09$) shown in Fig. 4. Pre-twisting and subsequent tension are analysed with the same m values.

where pre-twisting up to a moderate shear strain of $\Gamma = \Gamma_0 = 0.09$ was performed, which is typical of the room temperature experiments in [5]. These analyses have been carried out with the '400' grain distribution and have used a range of m values. The results in Fig. 4 and in particular the Swift effect shown in Fig. 4(b) agree qualitatively with the homogeneous shear results in [3]: the axial Swift effect decreases with increasing strain-rate sensitivity. A value of $m = 0.005$ appears to provide a close approximation of a rate-insensitive material. Figure 5 shows the effect of strain-rate sensitivity on the response to uniaxial tension from the corresponding pre-twisted and unloaded states. The shear strain Γ' and the axial strain ε' used to represent the tensile response are measured relative to the values of Γ and ε after unloading. It is seen that contrary to the torque response during pre-twisting, the axial force response increases with increasing value of m. The predicted inverse Swift effect is depicted in Fig. 5(b). During the initial elastic response, a very small amount of twisting in the same direction as pre-twisting is found due to the elastic anisotropy produced. When plastic slip starts to occur, for the smaller values of m, Γ' quickly decreases to negative values. After about twice the elastic regime ($\varepsilon' \approx 1\%$), however, twisting in the same direction as during pre-twisting starts again. The predicted untwisting behaviour is rather sensitive to the value of m; with $m = 0.2$ this untwisting has disappeared completely. The maximum amount of untwisting is observed in these cases for $m = 0.005$ where $\Gamma'_{\min} = -0.025\%$. At strains up to 20% the twisting response is found to be monotonic, but for even larger strains, the twisting direction may change again. However, this does not seem to bear any practical relevance as a maximum axial force is predicted to occur much earlier around $\varepsilon' = 5\%$, which indicates the onset of necking; but, clearly, this cannot be described by the present model.

In Fig. 6 we briefly study the effect of different moderate levels of pre-twist for a material with $m = 0.01$ and using the '400' grain distribution as in the previous figures. It is observed that increasing the amount of pre-twist, and therefore increasing the torsion texture, leads to a somewhat larger untwisting during tension, and which sustains larger tensile strains. Subsequent twisting in the same direction as pre-twisting appears to occur at roughly the same

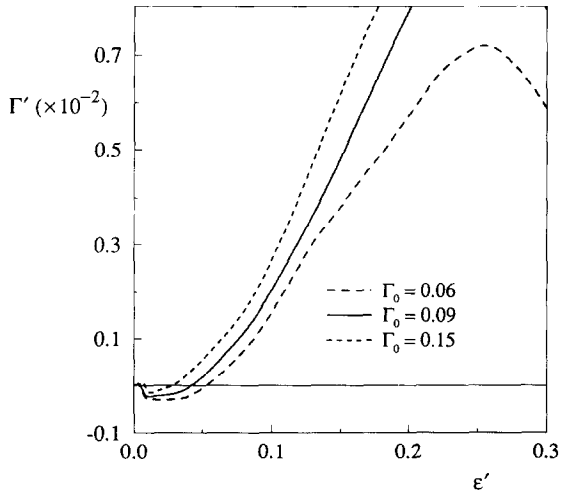

Fig. 6. Twist response during uniaxial tension from various, moderate strain pre-twisted states for $m = 0.01$ using the '400' grain distribution.

rate. In order to check the accuracy of the finite element discretization, we have repeated the analysis for $\Gamma_0 = 0.09$ with $n = 8$ elements instead of 5. The results differed by less than 1% from those shown in Figs. 5 and 6.

The previous results related to pre-twists involving moderate strains at which no strong textures have yet been formed in the material. Figures 7 and 8 show results for much larger shears up to $\Gamma_0 = 5$. The pre-twisting and unloading stages of these analyses have been carried out with $m = 0.05$, which is considered to be a typical value at elevated temperatures at which these large shears can be actually achieved in copper (cf., e.g., [3, 6, 22]). The tension computations have assumed the typical room temperature value $m = 0.005$. For completeness, Fig. 7 shows the response during free-end pre-twisting up to $\Gamma_0 = 5$, followed by unloading. These results are fully similar to those reported in [9]. The predicted Swift effect shown in Fig. 7(b), with a maximum value of $\varepsilon = 12\%$ at $\Gamma = 5$, agrees rather well with Swift's [1] experimental results for copper bars. As before, the computations used the '400' grain distribution, but the pre-twisting analyses have been repeated with the '300' and '500' grain distributions shown in Fig. 3. It is seen that for these large shears, the response is virtually insensitive to the initial orientation distribution; similar conclusions were reached for the homogeneous shear response in [3]. We shall return to the effect of initial texture later. The inverse Swift effect in these specimens with large pre-twists (see Fig. 8) exhibits a more complex phenomenology than the moderate pre-twist results of Fig. 6. With pre-twists of $\Gamma_0 = 0.5$ or $\Gamma_0 = 1$, no initial untwisting is observed at all, while for larger pre-twists of $\Gamma_0 = 2$ or $\Gamma_0 = 5$, untwisting is found again immediately after the onset of plasticity. This rather drastic change in response between $\Gamma_0 = 1$ and $\Gamma_0 = 2$ is probably due to texture changes that occur in between these shears, although the shear levels appear to be too small for the occurrence of abrupt changes in ideal texture components, as reported in [3].

In Fig. 9 we now study the effect of different initial grain distributions for a moderate level

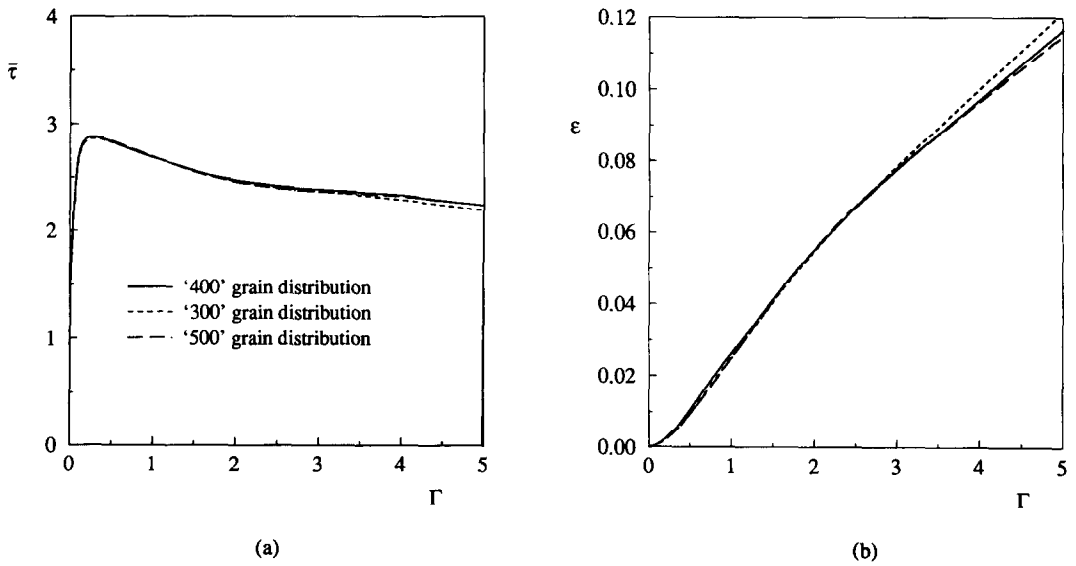

Fig. 7. Pre-twisting with $m = 0.05$ for various initial grain orientation distributions up to $\Gamma_0 = 5$ and subsequent unloading: (a) torque response, (b) axial strain development.

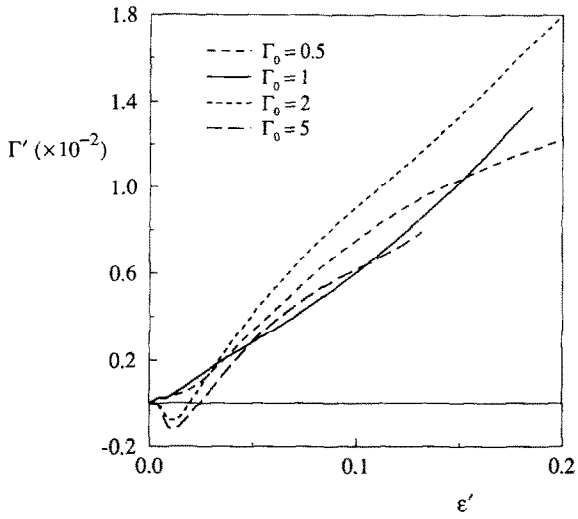

Fig. 8. Twist response during uniaxial tension with $m = 0.005$ from various, large strain pre-twisted states obtained with $m = 0.05$ (see Fig. 7) using the '400' grain distribution.

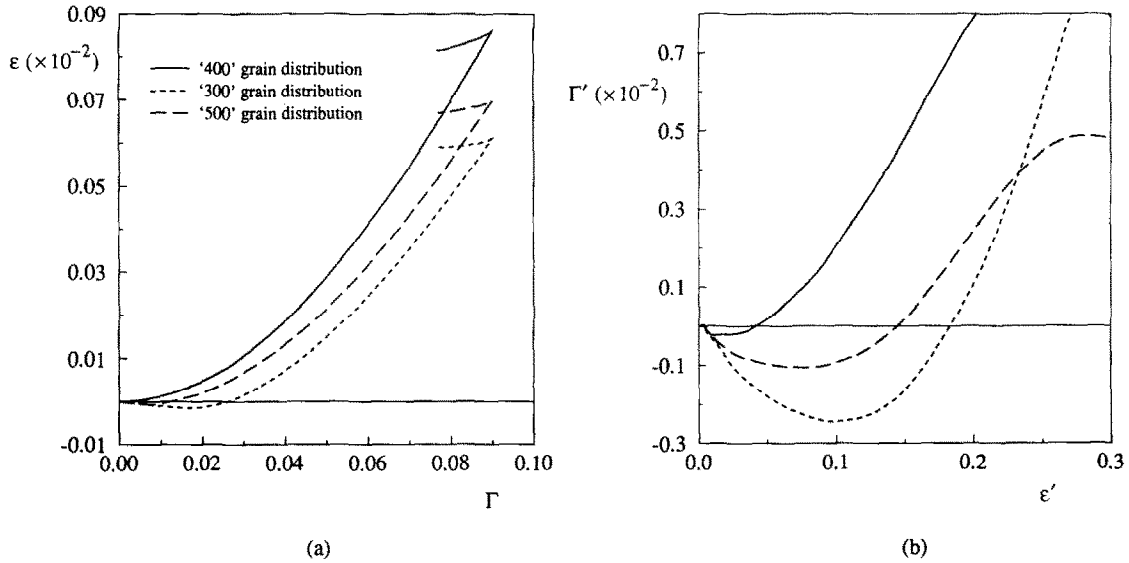

Fig. 9. (a) Axial strain development during pre-twisting with $m = 0.01$ until $\Gamma_0 = 0.09$ using various initial grain orientation distributions; (b) twist response during uniaxial tension from the corresponding pre-twisted states.

of pre-twist, namely $\Gamma_0 = 0.09$. The rate-sensitivity parameter m was taken equal to 0.01, and results for the '400' grain distribution have been shown before in Figs. 5 and 6. As we have noticed above in Fig. 7, the memory for the initial texture disappeared almost completely for large shear strains. However, Fig. 9(a) shows that in the moderate strain regime considered here, the axial strain development does turn out to be significantly affected by the initial texture, although no effect was observed on the torque response. In particular, the initial

shortening found with the '300' grain distribution is a notable effect of initial texture. The effect of using different orientation distributions on the subsequent inverse Swift effect is even stronger. Especially, the '300' grain distribution leads to a substantial untwisting which is about 10 times larger than with the '400' grain distribution and which persist until large axial strains of about 20%.

To get some more insight into the origin of this difference, we analyzed the problem of free extension of the initial material without pre-twisting, and found that both the '300' and the '500' grain distribution yielded significant amounts of untwisting at moderate to large strains: the minimum associated shear for the '300' grain distribution was $\Gamma'_{\min} = -0.44\%$ at $\varepsilon' = 16\%$, and $\Gamma'_{\min} = -0.19\%$ at $\varepsilon' = 12\%$ extension for the '500' grain distribution. These effects must be attributed to the fact that even though the grain distributions are random, they do not represent an isotropic aggregate, as already mentioned above. As a consequence of the procedure to generate the '400' grain distribution, that initial texture possesses all symmetries that are present in the applied tension mode of deformation (cf. [23]) and therefore shows no twisting at all during tension.

It is important to realize here that twisting of the solid bar involves radially inhomogeneous states of deformation and stress, and therefore produces an inhomogeneous texture. When the material is initially homogeneous and stress-free, the stress and deformation fields remain trivially homogeneous during uniaxial extension. On the other hand, when the material is inhomogeneously anisotropic due to a previous deformation history, as in the present simulations, certain regions in the bar will impose constraints on others so that the axial deformation be radially homogeneous. Thus, the precise variation of the textures due to pre-twisting along the radius will also contribute to the inverse Swift behaviour, but this cannot be easily quantified. Another contribution stems from the residual stresses in the bar after unloading. To get some insight in these residual stresses and the influence of the initial grain distributions, the stress state after unloading (stage II) from $\Gamma_0 = 0.09$ is plotted for the '300' and the '400' grain distributions in Fig. 10. The computations were carried out with $m = 0.01$, and the stress distributions are obtained by plotting the sampling point values of the σ_{11}, σ_{33} and σ_{23} components, with linear interpolation (the σ_{22} component is almost equal but

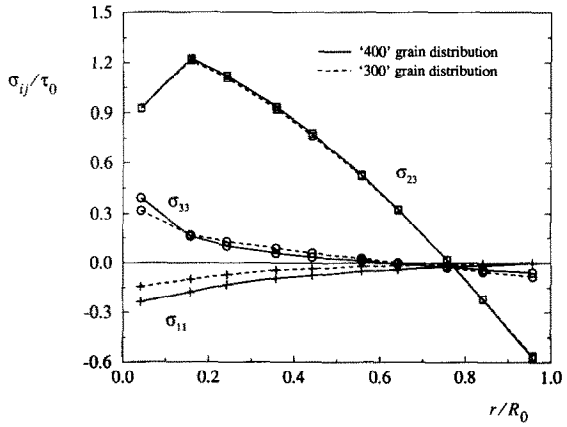

Fig. 10. Residual stress distributions across the bar after pre-twisting until $\Gamma_0 = 0.09$ and unloading, for two different initial grain distributions with $m = 0.01$.

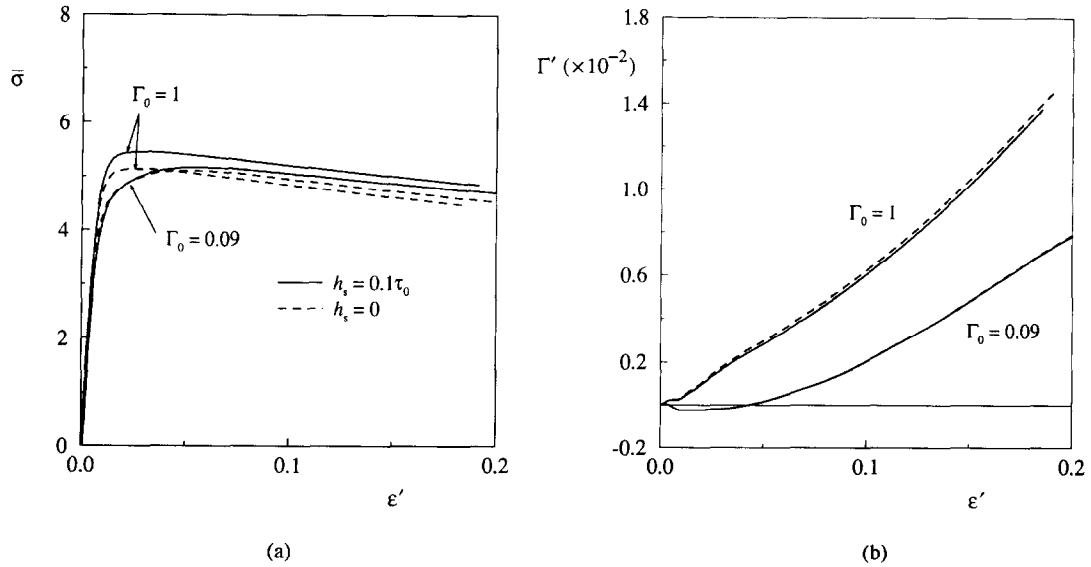

Fig. 11. Axial force response (a) and twist (b) during uniaxial tension illustrating the effect of strain hardening for two levels of pre-twist; $m = 0.01$ for all cases and the '400' grain distribution was used.

of opposite sign to σ_{11} and is not shown). The shear stress distributions indicate that for this level of pre-twist very little plastic deformation has taken place in the center of the specimen. It is observed that the normal stresses differ considerably between the two polycrystalline aggregates. This difference will also contribute to the difference in the subsequent inverse Swift effect observed in Fig. 9; but this influence is very hard to quantify as well.

It has been noted in relation to Fig. 5(a) that during tension, hardening is rapidly saturated and maximum axial load is attained at about 5% strain. This is much less than the strains at the onset of necking reported in [5] (see Section 2). Therefore, we have repeated two of the analyses with a nonzero value $h_s = 0.1\tau_0$ of the asymptotic hardening rate h_s; this same value has been used also in the homogeneous shear simulations in [3]. It has been found that with this value of h_s instead of $h_s = 0$ the axial stress response (see Fig. 11(a)) shows more hardening, as expected, but the twist response during tension (see Fig. 11(b)) is not significantly affected for either one of the two pre-twist levels of $\Gamma_0 = 0.09$ or $\Gamma_0 = 1$. The strain at maximum load, however, has not increased much.

6. Discussion and conclusion

The present analyses of free-end twisting, unloading and subsequent free-twisting extension of solid bars account for two important features: radial inhomogeneity of the stress and deformation fields, and crystallographic texture development. Our results have confirmed that textures produced during each of these stages are of prime importance for the inverse Swift effect, as put forward by Shrivastava et al. [5]. Moreover, we have found that this effect is very sensitive to the initial texture before pre-twisting, especially during the initial stages of plastic deformation in the extension stage and when the pre-twist has been performed up to

moderate shear strains of the order of 10%. This prompts further investigation with initial grain orientation distributions that better reflect the actual random distributions after annealing. The radial inhomogeneity of the stress and deformation fields can also be concluded to have a significant influence on the inverse Swift effect. In fact, it is not unlikely that the transient untwisting behaviour found in our simulations during the first stages of plastic extension are to a large extent due to this inhomogeneity in pre-twist textures and residual stresses.

For a thorough understanding of these effects, it seems pertinent to briefly point out some of the key consequences of the present modelling. First of all, it is essential to appreciate that the actual polycrystalline bar is replaced by a continuum, in which each volume element is supposed to represent a representative element of the polycrystalline aggregate under the Taylor assumption. The polycrystal constitutive equations attributed to each continuum element account for the distribution of lattice orientations in the representative polycrystalline aggregate, but cannot incorporate effects of grain shape and size, nor of its distribution. Secondly, by neglecting end effects of the bar, and assuming homogeneity of the material properties in the axial and circumferential direction, the actual 3-D problem is reduced to a 1-D problem. This means that any variation in the microstructure in axial or circumferential direction is not picked up by our model. In other words, each sampling point in the finite element model of the bar can be considered to really represent the behaviour of a tubular polycrystalline aggregate, averaged out over its length as well as over its cross-section. The orientation distributions of the grains attributed to a sampling point, addressed previously, should therefore correspond to the actual distribution in this tubular aggregate. A related issue is the role of the grain size relative to the dimensions of the specimen. It is inherent in the present continuum modelling that the grain size must be small compared to the radius of the specimen. The wires used in the experiments of Shrivastava et al. [5] had a radius of 0.5 to 1 mm, but, unfortunately, the grain size was not reported, so that the modelling assumptions cannot be verified. Nevertheless, the possibility that these assumptions are not fully justified for the wires used in [5] has to be born in mind when comparing the numerical results with the experimental results.

Confronting, for comparable deformation histories, our results with the experimental findings of [5] shown in Fig. 1, it must be concluded that the agreement is not very satisfactory. The experimental results obtained with pre-twisting at elevated temperature should be left out of such a comparison, because dynamic recrystallization is in no way accounted for in our model. Comparing the typical room temperature result in Fig. 1 with our results in for instance Figs. 5, 6 and 9, we observe two main differences. First, the experimental initial untwisting behaviour after a moderate pre-twist seems to be more pronounced than found here with an orientation distribution that respects the symmetries of the uniaxial deformation field. As suggested in [5], there may be a significant Bauschinger effect or some kinematic hardening involved, which manifests itself during the strain path change from torsion to extensions. This has been completely ignored in the present model. In order to check this hypothesis, the slip system hardening law will have to be augmented with the possibility of kinematic hardening, such as the model proposed in [24].

The second main difference with the experimental results is that the inverse Swift effect at larger extensions, $\varepsilon > 0.1$ say, tends to be overestimated by our model. Only with a value of the rate sensitivity parameter m of 0.2 can we obtain a reasonable quantitative agreement with

the experiment data in Fig. 1, but this value is considered to be too large for room temperature. One of the possible causes for this discrepancy may be that the Taylor assumption, where all grains are subjected to the same overall deformation, is a poor approximation at large extensions. Indeed, it is well-known that the Taylor assumption tends to predict excessively sharp textures (cf. e.g. [2]). The implementation of a self-consistent model (e.g. [25]) into the finite element model may give some insight in the importance of this aspect in explaining the inverse Swift effect. Another aspect that may be related with this discrepancy is that the strain at maximum load predicted by our computations is considerably smaller than the strain at necking observed in the experiments. This seems to suggest that the single crystal hardening description may not be adequate. A possible source for this, evidently, is that the set of hardening parameters used in the analyses does not describe the material of [5] sufficiently accurately. In addition, the hardening model employed here in (11) is admittedly a rather simple one. It involves purely isotropic hardening for all slip systems in the crystal, thus neglecting latent hardening which is well-known to be a very important factor (see e.g. [3, 26]). More refined hardening models that account for latent hardening in crystallites have been proposed in the literature (see, e.g., [27–29]) very recently; a further study of the inverse Swift effect on the basis of such models will be reported in the future.

Acknowledgment

We are indebted to S.C. Shrivastava for supplying us with the results shown here in Fig. 1, which were taken from [5]. KWN gratefully acknowledges the financial support of NSERC (Canada) and FCAR (Québec).

References

[1] H.W. Swift, Length changes in metals under torsional overstrain, Engineering 163 (1947) 253–257.
[2] J. Gil-Sevillano, P. Van Houtte and E. Aernoudt, Deutung der Schertexturen mit Hilfe der Taylor-Analyse, Z. Metallkunde 66 (1975) 367–373.
[3] S. Harren, T.C. Lowe, R.J. Asaro and A. Needleman, Analysis of large-strain shear in rate-dependent face-centered cubic polycrystals: Correlation of micro- and macromechanics, Philos. Trans. Roy. Soc. London Ser. A 328 (1989) 443–500.
[4] L.S. Tóth, J.J. Jonas, D. Daniel and J.A. Bailey, Texture development and length changes in copper bars subjected to free end torsion, Textures and Microstructures 19 (1992) 245–262.
[5] S.C. Shrivastava, J.J. Jonas and L.S. Tóth, The inverse Swift effect in pretwisted and freely extended wires, in: T.C. Lowe, A.D. Rollett, P.S. Follansbee and G.S. Daehn, eds., Modeling the Deformation of Crystalline Solids (The Minerals, Metals and Materials Society, 1991) 205–208.
[6] K.W. Neale, L.S. Tóth and J.J. Jonas, Large strain shear and torsion of rate-sensitive FCC-polycrystals, Internat. J. Plast. 6 (1990) 45–61.
[7] R.J. Asaro and A. Needleman, Texture development and strain hardening in rate dependent polycrystals, Acta Metall. 33 (1985) 923–953.
[8] P.D. Wu and E. Van der Giessen, Analysis of elastic-plastic torsion of circular bars at large strains, Arch. Appl. Mech. 61 (1991) 89–103.
[9] E. Van der Giessen, K.W. Neale and Y. Qiu, Analysis of the Swift effect in solid bar torsion using a rate-sensitive crystal plasticity model, in: S.I. Andersen et al., eds., Modelling of Plastic Deformation and its Engineering Applications (Risø, Roskilde, Denmark, 1992) 479–484.

[10] D. Peirce, R.J. Asaro and A. Needleman, Material rate dependence and localized deformation in crystalline solids, Acta Metall. 31 (1983) 1951–1976.
[11] J.R. Rice, Inelastic constitutive relations for solids: An internal variable theory and its applications to metal plasticity, J. Mech. Phys. Solids 19 (1971) 433–455.
[12] R.J. Asaro and J.R. Rice, Strain localization in ductile single crystals, J. Mech. Phys. Solids 25 (1977) 309–338.
[13] J.F. Besseling, A thermodynamic approach to rheology, in: H. Parkus and L.I. Sedov, eds., Proc. IUTAM Symp. on Irreversible Aspects of Continuum Mechanics (Springer, Wien, 1968) 16–53.
[14] J. Mandel, Plasticité Classique et Viscoplasticité, CISM Lecture Notes No. 97, Udine (Springer, Berlin, 1971).
[15] E. Van der Giessen, Some aspects of the macroscopic plastic spin during texture development in polycrystalline metals, in: G.Z. Voyiadjis, ed., Microstructural Characterization in Constitutive Modeling of Metals and Granular Media, MD-Vol. 32 (ASME, New York, 1992) 5–19.
[16] S.C. Shrivastava, J.J. Jonas and G. Canova, Equivalent strain in large deformation torsion testing: Theoretical and practical considerations, J. Mech. Phys. Solids 30 (1982) 75–90.
[17] L. Delhage, Strain-rate and axial effects during reversed large strain torsion of solid circular bars, Delft Univ. of Techn., Lab. for Engrg. Mech. Report no. 924, 1990.
[18] E. Van der Giessen, Some remarks on the analysis of large strain torsion-like problems, Acta Mech. 89 (1991) 233–239.
[19] K.K. Mathur and P.R. Dawson, On modeling the development of crystallographic texture in bulk forming processes, Internat. J. Plast. 5 (1989) 67–94.
[20] D.R.J. Owen and E. Hinton, Finite Elements in Plasticity: Theory and Practice (Pineridge, Swansea, 1980).
[21] E. Van der Giessen, P.D. Wu and K.W. Neale, On the effect of plastic spin on large strain elastic-plastic torsion of solid bars, Internat. J. Plast. 8 (1992) 773–801.
[22] F. Montheillet, P. Gilormini and J.J. Jonas, Relation between axial stresses and texture development during torsion testing: A simplified theory, Acta Metall. 33 (1985) 705–717.
[23] P. Van Houtte and E. Aernoudt, Considerations on the crystal and the strain symmetry in the calculation of deformation textures with the Taylor theory, Mater. Sci. Engrg. 23 (1976) 11–22.
[24] L. Méric and G. Cailletaud, Single crystal modelling for structural calculations: Part 2 – Finite element implementation, J. Engrg. Mat. Techn. 113 (1991) 171–182.
[25] A. Molinari, G.R. Canova and S. Ahzi, A self-consistent approach of the large deformation polycrystal viscoplasticity, Acta Metall. 35 (1987) 2983–2994.
[26] U.F. Kocks, The relation between polycrystal deformation and single-crystal deformation, Metall. Trans. 1 (1970) 1121–1143.
[27] J.L. Bassani, Single crystal hardening, Appl. Mech. Rev. 45 (1990) 320–327.
[28] A.M. Cuitiño and M. Ortiz, A dislocation model of work hardening in ductile single crystals, in: C. Teodosiu, F. Sidoroff and J.L. Raphanel, eds., Large Plastic Deformations – Fundamentals and Applications to Metal Forming, Proc. MECAMAT'91 (Balkema, Rotterdam) (in press).
[29] Y. Zhou, K.W. Neale and L.S. Tóth, A modified model of latent hardening for rate-dependent FCC polycrystals, Internat. J. Plast. (submitted).